# WAVELET CONDITIONING FOR AXIAL STRAIN TIME CONSTANT ESTIMATION

A Thesis

by

PALLAVI PREMKUMAR

Submitted to the Office of Graduate and Professional Studies of
Texas A&M University
in partial fulfillment of the requirements for the degree of

MASTER OF SCIENCE

| | |
|---|---|
| Chair of Committee, | Raffaella Righetti |
| Committee Members, | Xiaoning Qian |
| | Jun Zou |
| | J.N Reddy |
| Head of Department, | Miroslav M. Begovic |

August 2019

Major Subject: Electrical Engineering

# ABSTRACT

Ultrasound elastography has gained considerable consideration as a non-invasive imaging modality over the past ten years. Ultrasound elastography maps the strains experienced by a tissue under a small compression with the intent of acquiring diagnostic information about diseases. Elastographic data acquired from function-specific imaging mode can be utilized to distinguish tissue stiffness when subjected to a small external mechanical force. Poroelastography is a new elastographic technique that is used to image the temporal behavior of tissues subjected to a small uni-axial mechanical force. From the temporal data, poroelastographic imaging makes use of curve fitting techniques to estimate temporally-related elastographic parameters such as the Axial Strain Time Constant (ASTC). Curve fitting techniques can be directly applied to ultrasound data obtained from the soft tissue subjected to a constant compression. However, experimental poroelastographic data are inherently noisy due to long, oftentimes hand-held, data acquisition. The presence of this noise can affect the accuracy of the ASTC estimation. To estimate the ASTC with high accuracy, it is essential to reduce the noise that affects the data before applying the curve-fitting techniques. This work focuses on a method to denoise ultrasound poroelastographic data, which uses wavelet thresholding in order to improve the robustness of the curve fitting technique and increase the accuracy of the estimated ASTC. Wavelet thresholding is achieved through evaluating the wavelet coefficients and choosing the threshold optimally. Threshold value determines the efficiency of the denoising operation. In this work, we are using wavelet filtering along with the wavelet hard thresholding technique. Simulations are used to test the proposed denoising methods. Experiments were used to demonstrate the applicability of the proposed technique to experimental data. Simulation results show that the use of the wavelet-based denoising method prior computation of the ASTC using curve fitting can lead to ASTC estimates that are significantly more accurate than those obtained when the denoising method is not used.

# DEDICATION

To my loving husband, Madhava Keralapura, for his unfailing support and unceasing encouragement. To my parents, M S Premkumar and Jayashree Premkumar, for their unconditional love and support.

# ACKNOWLEDGMENTS

I would like express my heartfelt gratitude to my thesis advisor, Dr. Raffaella Righetti, for her time, patience and valuable guidance. She has been a constant source of inspiration throughout my course of study. Apart from my advisor, a special shout-out to my thesis committee: Dr. Xiaoning Qian, Dr. Jun Zou and Dr. J.N Reddy for their encouragement.

I would like to extend my gratitude to MD Tauhidul Islam, who consistently steered me in the right direction and helped me to widen my research perspectives when needed. I would also like to thank my fellow lab-mate, Songyuan Tang, for all the brain storming discussions, experimental guidance, and feedback.

Last but foremost, I am grateful to the unfailing support extended by my family and friends during my Master's degree program.

CONTRIBUTORS AND FUNDING SOURCES

## Contributors

This work was supervised by my thesis chair and advisor, Dr.Raffaella Righetti. The Finite Element simulation data used for Chapter 06 was provided by MD Tauhid Islam.

All other work conducted for the thesis was completed by the student independently.

## Funding Sources

No outside funding was received for the research and compilation of this document.

# NOMENCLATURE

| | |
|---|---|
| ASTC | Axial Strain Time Constant |
| EPR | Effective Poisson Ratio |
| TC | Time constant |
| RF | Radio Frequency |
| LM | Levenberg - Marquardt |
| LSE | Least Square Error |
| GLSE | General Least Squared Error |
| SLSE | Standard Least Square Error |
| WT | Wavelet Transform |
| WC | Wavelet Conditioning |
| CF | Curve Fitting |
| RAM | Random Access Memory |
| AM | Amplitude Modulation |
| SNR | Signal to Noise Ratio |
| PSNR | Peak Signal to Noise Ratio |
| MSE | Mean Sqaure Error |
| BW | Bandwidth |

TABLE OF CONTENTS

Page

LIST OF FIGURES

FIGURE Page

LIST OF TABLES

TABLE Page

# 1. INTRODUCTION

Elastography is an ultrasound imaging modality capable of imaging the local mechanical response of a tissue subjected to a small compression [1]. Elastography provides additional diagnostic information compared to standard ultrasound methods. Elastography imaging modality consolidates transducer pressure with ultrasound to give clinical guidance about the state or presence of the disease, severity of the disease and status of the tissue under treatment. The extent to which the pathological tissue resists deformation in response to an applied mechanical force can be relatively different compared to the surrounding healthy tissue [2] [3]. Ultrasound elastography therefore takes advantage of these changed differences in the underlying mechanical properties to differentiate a diseased tissue from healthy normal tissue. Quasi-static ultrasound elastography maps the strains experienced by the tissue during the compression. Dynamic elastography, instead, maps the strains experienced by the tissue either by analyzing the strain induced in the tissue under small compression, or by the imaging the tissue when excited using low frequency vibrations or shear waves [1]. The strains are computed by correlating the pre-compressional and post-compressional RF data. An Axial strain elastograms represents a map of the strain tensor component along the axis of the imaging plane [2]. For the interpretation of standard elastographic images, biological tissues are typically modeled as linear elastic and in-compressible solids [4]. In reality, several tissues in our body contain fluid and they change volume when subjected to compression [5]. Poroelastography is an advanced elastographic imaging technique where the tissue is modeled as a biphasic material - somewhat similarly to a sponge [6]. When a poroelastic tissue is subjected to a small sustained compression, the elastic properties of the tissue change due to solid matrix deformation or fluid translocation [7] [8]. Poroelastographic imaging is interested in imaging the time-dependent deformation of the tissue when subjected to the sustained compression such as during a creep relaxation experiment or a stress relaxation experiment[8]. Poroelastography techniques allow the generation of new types of elastograms concerning the tissue's poroelastic behavior. [2].

Axial strain elastograms are sensitive to the strain in the tissue under loading along the axis of the imaging plane. Poroelastographic imaging generates time-sequenced axial strain elastograms when poroelastic tissue is subjected to creep or stress relaxation [2] [9]. Time-sequenced axial strain elastograms are used to analyze temporal behavior of the pixel, pixel-by-pixel basis and compute time constant to generate ASTC elastogram. ASTC differences are typically associated with inherent differences in tumor and ordinary tissue's mechanical characteristics [10]. Studies have shown that ASTC may provide significant, clinically relevant information to distinguish the diseased tissue from the normal tissue and to predict the probable outcome of a disease or ailment [2]. ASTC values were also found to correlate with the state or presence of malignant breast cancer. [9][2][10]. Hence accurate assessment of ASTC may be important for clinical applications.

### 1.1 Motivation

Prior work on ASTC imaging has led to the development of a real-time ASTC estimator using Curve fitting and optimization techniques [9]. The curve fitting technique works extremely well as an ASTC estimator when applied to simulated data modeled with only additive Gaussian noise. However, axial strain ultrasound data may be corrupted by additional types of noise, for instance - multiplicative noise [11]. Unfortunately, the curve fitting technique fails to estimate ASTC accurately when directly applied to ultrasound simulated noisy data.

### 1.2 Hypothesis

The hypothesis of this study is that we can improve the performance and robustness of the curve fitting technique to estimate the ASTC values closer to the true value, by denoising the poroelastographic data using wavelet thresholding.

### 1.3 Research Plan

- Design and implement a denoising algorithm to improve accuracy in the estimation of ASTC.
- Evaluate the reliability and performance of the algorithm using a simulation framework.
- Conduct suitable experiments as a proof of concept.

# 2. ULTRASOUND IMAGING

## 2.1 Ultrasound Overview

Ultrasound is an acoustic wave with frequencies higher than human audible range. Ultrasound imaging is a noninvasive imaging modality that uses ultrasonic waves and their echoes to obtain anatomical view of the body and diagnose, monitor and treat tissues. Ultrasonic frequency range for medical instrumentation to achieve good resolution and good penetrability, is from 0.5MHz to 20MHz. Changes in brightness in ultrasound image depend on the intensity of the back-scattering coefficient. During transmission, the transducer converts electrical signals into ultrasonic waves and during reception, it converts received ultrasonic echoes into electrical (RF) signals. Ultrasonic transducer is placed on the surface of the skin or inserted into a body opening to obtain visual representation of the inside of a body.

## 2.2 Elastography Overview

Ultrasound Elastography is interested in imaging the local mechanical response of the tissue, when tissue is subjected to small sustained compression. Tissue elasticity imaging can be characterized based on the mechanical stimulus propagated into the tissue, 1) Quasi-static elastography where a small mechanical compression is used to image the strain experienced by the tissue [12] [13] [14] 2)Dynamic elastography where low-frequency vibration/ultrasound harmonic pulses are used to inspect the behavior of the tissue [15] [16] [17] [18] [19]. In this work, strain elaastography is discussed briefly. Strain elastography or standard elastography is based on quasi-static tissue strain estimation [20]. When a tissue is compressed using a constant uni-axial load, stiff and soft tissue regions experience different strain levels [21]. The extent to which a diseased tissue resists deformation in response to an applied mechanical force is relatively different compared to a surrounding healthy tissue [2] [3]. Ultrasound strain elastography therefore takes advantage of these changed mechanical properties to differentiate the diseased tissue from healthy normal tissue. From knowledge of the elastographic strains generated into the tissue, mechanical attributes

of the tissue may be reconstructed [11]. These may include the shear or Young's modulus or the Poisson's ratio [20]

### 2.2.1 Strain Elastography Working Principle

1. Acquire pre-compression RF data from the region of interest.

2. Apply a small sustained compression using ultrasonic transducer along with the compression plates to compress tissue by a small amount.

3. Acquire post-compression RF data from the same region of interest.

4. Estimate the strain using pre-compressional and post-compressional RF data. Numerous strain estimation algorithms algorithms have been proposed in the past. In this work, we have used dynamic programming elastography (DPE) and Horn-Schunck (HS) optical flow estimation [22] based strain estimation.

Axial strain elastograms represent images of the strain tensor component along the axis of the imaging plane [9]. Axial strain elastograms represent the mechanical attributes of the tissue in a qualitative way. With the use of wide bandwidth transducers and fast sampling of the ultrasonic RF signals, axial strains can be estimated with high degree of precision [21]. In general, lateral strain elastograms are noisier than axial strain elastograms and their precision is restricted due to the relatively small lateral sampling rate [21]. Elastographic techniques are clinically useful in several types of medical applications, such as cancer imaging, early diagnosis of lymphedema, kidney and liver diseases [2] [23].

## 2.3 Poroelastography Overview

Novel elastographic techniques aimed at imaging tissue's temporal mechanical behavior have been recently proposed [8]. Among these, viscoelasticity imaging and poroelastography are the most prominent ones. Most of our work is focused on poroelastography. Therefore, remainder of this chapter will concentrate on the fundamental ideas and applications of poroelastography imaging. True incentive behind these new elastographic techniques originates from the profound assess-

ment that several pathologies modify the temporal mechanical response of the tissue [2]. Poroelastography makes use of elastographic techniques for imaging the temporal mechanical behavior of poroelastic materials when subjected to small sustained compression [8]. In Poroelastography, biological tissues are modeled as biphasic systems - similar to a sponge [6]. A poroelastogram is defined as a series of temporally sequenced elastograms obtained from the tissue under load at different intervals [20]. Poroelastograms reveal information about the temporal mechanical behaviour of the poroelastic tissue [24] [25]. Poroelastography techniques allow generation of new types of elastograms that are related to the tissue's poroelastic behavior.

### 2.4 Axial Strain TC Estimation

Poroelastographic imaging generates series of temporally sequenced axial strain elastograms when poroelastic tissues are subjected to a constant axial strain or constant axial stress [2]. These Time-sequenced axial strain elastograms are used to analyze temporal behavior of the pixel and compute time constant pixel-by-pixel to generate ASTC elastogram [20]. ASTC elastograms reflect temporal modifications in poroelastic tissue due to translocation of fluids. ASTC is obtained by calculating the time constant of the exponential increase of the axial strain over the time interval of the poroelastogram [20]. It is plausible to use several conceptual models to obtain tissue time constants from the stress relaxation data or creep relaxation data [26] [27]. Therefore, simplistic exponential polynomials that uses multiple exponential terms can serve as an appropriate option to approximate creep relaxation data or stress relaxation data for clinical applications [23] [5] [9] [11].

# 3. STRAIN MODEL

Time constant $\tau$ and the equilibrium value $\eta$ rely heavily on the imaging tissue or the material and could be vital for diagnostic purposes. When data is collected for an infinite amount of time without any noise, estimating the $\tau$ would be fairly straightforward. In reality, however, the ultrasound data is heavily corrupted by noise. Furthermore, it may be a major challenge to obtain ultrasound data for indefinite amount of time, especially in clinical setting. The strain behavior is comparable to the voltage response of Resistor Capacitor circuit [28]. The strain is sampled at Nyquist rate and $N_i$ is additive Gaussian noise with zero - mean distribution.

Two major types of noise predominantly corrupt the creep data. One is the decorrelation noise, another is the amplitude modulation noise [29]. Compression, slide-slippage, and other undesirable movement in the sample can induce decorrelation noise [11]. An arbitrary variation in the RF signal magnitude can induce amplitude modulation noise [11]. The Amplitude modulation noise shifts the strain estimation from the center of the observation window, resulting in incorrect estimates [11]. Decorrelation noise, is modeled as additive Gaussian noise [9] [30] [31], whereas AM noise is modeled as multiplicative noise similar to speckle noise in B-mode ultrasound [11]. The generic strain model is given below [11].

$$S_i = I_i + N_i \tag{3.1}$$

where, $I_i = V_i * Z_i$ and $Z_i = \eta + \gamma e^{\frac{-t_i}{\tau}}$

$Z_i$ is the true strain, $V_i$ is the multiplicative noise and $N_i$ is the additive Gaussian noise in the strain data. $\gamma$ is adapted accordingly to suit the poroelastic material strain model [11]. In this study we will consider multiplicative noise along with additive Gaussian noise.

# 4. CURVE FITTING AND OPTIMIZATION

## 4.1 Introduction

Curve fitting refers to finding an appropriate mathematical model that expresses the relationship between a dependent variable Y and a single independent variable X and estimating the values of its parameters using nonlinear regression. The curve fitting problem typically involves comparing a theoretical noiseless test curve to the noisy experimental data and find the best fit to a series of data points in noisy experimental data subjected to certain constraints. The real-time ASTC estimator developed in our lab [9] uses the least square error curve-fitting method along with the LM optimization directly applied over the noisy elastographic data.

## 4.2 Least Square Error

LSE curve fitting is an extremely popular data fitting method. The best fit is considered to be the one with the smallest error between an observed value and the fitted value. In Least Square Error technique, the observational errors on both dependent and independent variables are considered. The mathematical model for LSE that minimizes the error for $\eta$,$\tau$ is:

$$LSE\left(y\left(t,\eta,\tau\right)\right)=\sum\nolimits_{i=1}^{n}E(y\left(t,\eta,\tau\right),S\left(t_{i}\right)) \tag{4.1}$$

Where $E(y(t,\eta,\tau),S(t_i))$ gives the smallest error between an observed value and the fitted value, n refers to the set of data points.

### 4.2.1 General Least Square Error

General Least Square Error curve fitting involves minimization of the geometric error. It is called the geometric error because it is the minimum Euclidean distance between the experimental data point and the plot of a given noiseless theoretical error [9]. Main issue with GLSE technique is, modification in the scaling of the strain vs. time plot changes the results of the best fit. Furthermore, since the calculation of the error metric for each data point involves the computation of a minimum

which in turn can deteriorate the computation speed.

### 4.2.2 Standard Least Square Error

Standard Least Square Error curve fitting involves minimization of the algebraic error. Unlike GLSE, plot scaling has no effect on the resulting estimation. Standard Least Square Error is best suited for scenarios in which the noise model for the data samples acquired is Gaussian [9]. The mathematical model for SLSE that minimizes the error for $\eta$ ,$\tau$ is:

$$E(y\,(t,\eta,\tau)\,,S\,(t_i)) = (y\,(t) - S\,(t_i))^2 \tag{4.2}$$

## 4.3 LM Optimization

Mathematical optimization is the method of choosing the best element from the available series of possibilities with regard to some criterion. In general, an optimization problem consists of maximizing or minimizing a function whose domain is in real numbers $\mathbb{R}$ by trial and error method. The LM Optimization algorithm is an iterative algorithm appropriate for non-linear least square problems. These minimization problems occur mainly in least square curve fitting [32] [33] [34]. Berry et al. [23] used the LM optimization algorithm previously for poroelastographic imaging purposes. LM optimization is based on gradient descent and the Gauss-Newton [32].

However, LM optimization method is more robust than the Gauss-Newton algorithm. LM optimization method estimates the Hessian matrix using the sum of outer products of the gradients. One of the shortcomings of LM optimization approach is, it finds only a local minimum, which is not necessarily the global minimum. LM optimization follows an update rule of the form [32],

$$x_{k+1} = x_k - (H + \lambda I)^{-1}\,\nabla E(x_k) \tag{4.3}$$

where $x_k$ is the current guess and is given by, $[\tau_k, \eta_k]^T$. H is the hessian of $E(x_k)$ . "I" denotes a diagonal matrix and is given by diag(diag(H). $E(x_k)$ denotes the gradient of $E(x_k)$. $\lambda$ is a constantly changing step size. It is possible to increase or decrease $\lambda$ to accept or reject the update

and it affects the rate of convergence of the algorithm.

For a given set of temporal strain samples free of AM noise, the LM optimization algorithm implemented for the SLSE goodness of the fit argument estimates the best $\eta$ and $\tau$ pair. In this study we are mainly focusing on $\tau$, ASTC.

# 5. WAVELET CONDITIONING

## 5.1 Introduction

Wavelet transform is one of the dominant tool for reducing the effect of multiplicative noise from ultrasound data. Wavelet Transform is used for representation and analysis of function at more than one resolution [35]. Fourier transform based methods fail to perform well while working on non-stationary signals and they capture only the global features [36]. In practical scenario where the data are only piece-wise smooth and the noise distributions are random in nature, Wavelet transform perform better than Fourier filters on multiplicative noise [36]. Individuals have more option and control in the wavelet domain and can basically identify the frequency transients in the decomposed bands that would otherwise be removed by conventional fourier filtering or we can denoise a few decomposed bands and leave other decomposed bands alone.

### 5.1.1 Algorithm Overview

The main idea is shown in the Figure 5.1 (adapted from [37] [38]). In the analysis step the signal is decomposed into wavelet coefficients for analysis. In the processing step we perform wavelet thresholding to denosie the data and the denoised decomposed data is reconstructed in the synthesis step. Analysis and synthesis step is analogous to Filter bank.

The general application of wavelet thresholding to our elastography problem comprises the following steps:

1. Performing multilevel 1D wavelet analysis on the noisy Elastographic data to get the wavelet coefficients (approximation coefficient and detail coefficients).

2. Estimate the noise level from the detail wavelet coefficients.

3. For detail coefficients,

   (a) Calculate the standard deviation and threshold

   (b) Apply thresholding to remove high frequency noise components

4. Apply Low pass filtering on approximation coefficients to remove small noise coefficients and capture signal components around DC , in order to obtain perfect denoised reconstruction.

5. Reconstructing the denoised data by multilevel 1D Wavelet reconstruction.

6. Apply LSE curve fitting with LM optimization to the reconstructed denoised elastographic data to estimate the ASTC elastographic parameter accurately.

The thresholding is applied to the detail coefficients and Low pass filtering is applied to the approximation coefficients in the wavelet domain. This creates an algorithm that is easy and computationally more effective to remove multiplicative noise [39] [40].

### 5.2 Multilevel 1-D Wavelet Decomposition

Given a signal of length N, the signal can be decomposed into log(to the base 2)N levels, maximum [38]. Decomposition up-to maximum level is required for perfect denoised reconstruction of the signal. The first step decomposes the signal into approximation coefficients, and detail coefficients. Approximation coefficients are obtained by convolving the signal with the low pass wavelet filter. Similarly, convolving the signal with the High pass filter we can obtain the detail coefficients [38]. the filter outputs are down sampled by a factor of 2. The high pass and low pass filters produce signals by spanning only half the frequency band at each level of decomposition and thus reducing the frequency uncertainty by half. The down sampler is used in order to compress the data and obtain even indexed convolution.


Figure 5.1: Denoising Overview

The next step splits the approximation coefficients in two parts using the same scheme, replacing signal by the first approximation coefficient, and producing second level approximation coefficients and detail coefficients, and so on [38].

### 5.3 Wavelet Thresholding

Approximation coefficients contain low-frequency terms which in turn contain significant signal components and therefore less affected by noise. A low pass filter is used to filter the approximation coefficients to capture the frequencies around DC and remove any noise remnants present in the signal. Since the noisy components are of high frequency, approximation coefficients are less affected by noise compared to detail coefficients. Therefore, thresholding is usually limited to the detail coefficients. Hence, with the help of proper threshold we can remove the noisy components and can smooth the noisy wavelet coefficients. If the threshold value is low, noise components may still be present in the estimated signal. Whereas, if the threshold is high then the signal is over smoothed, hence result in loss of important signal components. Therefore, optimal threshold selection is crucial for the performance of denoising algorithm.

A brief overview of two popular thresholding algorithms, hard and soft thresholding, are presented in this section. The hard thresholding algorithm follows, maintain or destroy strategy. It sets any coefficient less than or equal to the threshold to zero refer Figure [41]. On the other hand, the soft thresholding algorithm, also known as wavelet shrinkage, sets any coefficient less than or equal to the threshold to zero [42] and the threshold is subtracted from any coefficient that is greater than the threshold [38]. This moves the image coefficients toward zero [42] [36].

The general equation to compute threshold value $T_n$ is given by [43] [44],

$$T_n = \frac{\gamma\sigma^2}{\sigma x} \tag{5.1}$$

where $\gamma$ is the scale factor, $\sigma x$ is the standard deviation of the detail coefficients and $\sigma^2$ is the variance of the detail coefficients [45]. The scale factor $\gamma$ is calculated for each decomposed using the equation below,

$$\gamma = \sqrt{\log(\frac{L}{D_L})} \tag{5.2}$$

where $L_i$ in the numerator represents the length of the detail coefficients at $i^th$ level, $D_L$ in the denominator represents the total number of wavelet decomposition.

Noise variance $\sigma^2$ is estimated using equation below [37].

$$\sigma \quad = \left[\frac{median\left(|Yij|\right)}{0.6745}\right]^2 \tag{5.3}$$

where, $Yij \in$ detail Coefficients.

The experimental factor 0.6745 in the denominator re-scales the numerator so that $\sigma^2$ is a suitable estimator for the $\sigma$ for the noise [37].

### 5.4 Multilevel 1-D Wavelet Reconstruction

Before wavelet reconstruction we apply Low pass filtering on Approximation coefficients and remove all the detail coefficients except the last level. This is important as we are dealing with small strain data in the order of 1-2%. In the synthesis stage up-sampler is used to compensate for downsampling done at analysis stage. First upsample by a factor of 2 and then convolve the signal with a known inverse filter. Same concept can be extended for multilevel.

# 6. SIMULATION METHODS

Simulating the noisy time constant curves and using the simulated data as an input for the time constant estimator algorithm, we test the performance of the proposed algorithm. Simulations are used to test the hypothesis of this study. Although several denoising algorithms have been tested, only wavelet conditioning is recorded as it is the most relevant real - time constant estimators discussed in this study. 1D simulation analysis was carried out to evaluate the accuracy, precision and performance of the algorithm as a function of the true time constant value of the axial strain. Because of the noise model's importance in the estimation process, selected simulations have been repeated for different input SNR values.

## 6.1 MATLAB Simulation

All simulations were conducted using a desktop computer with windows 10 Operating system. The desktop computer had following specification, Intel(R) Xeon(R) Gold 6148 CPU @ 2.40 GHz 2.39GHz, 2 processors, 5 GB RAM. A simulation model using MATLAB- R2018b, academic use was used to run the simulations and evaluate the algorithm. For simulation, an empirical axial strain curve with known $\eta$ and $\tau$ values were created using MATLAB according to the generic strain model given in the chapter 3. All the MATLAB simulations in this study use values of $\eta = 0.25$ and $\tau = 60s$. Once the empirical axial strain curve was created both AM noise and decorrelation noise were added to it accordingly to perform ASTC estimation. For statistical analysis, 100 trials were run. Figure 6.1 gives an overview of the MATLAB simulation flow employed for both the methods for comparison in our study.

Figure 6.2a is a example of noise free empirical axial strain curve used for the simulation study. Figure 6.2b illustrates the effect of adding noise to an empirical strain curve with a TC of 60 seconds and $\eta = 0.05$ such that the resultant noisy curve has a Input SNR of 20dB

Once the noise has been added to an empirical curve for a specific TC, the theoretical curve is discarded, leaving only the noisy curve for TC estimation. This process is repeated n times,

giving 'n' TC estimates to analyze. Once 'n' TC estimates have been obtained, the accuracy of the estimator is measured. Here 'n' indicates the number of trials. For statistical analysis, 100 trials were run. The example of a simulation run for a single realization is show in the Figure 6.3.

### 6.2 Finite Element Method

Analyzing a problem using finite element method is called Finite Element Analysis (FEA). We have used ABAQUS FEA software suite for finite element analysis in our study. ABAQUS FEA software suite is developed by Abaqus Inc, Rhode Island, United States. ABAQUS FEA software offers powerful and complete solutions for both routine and sophisticated engineering problems covering a vast spectrum of industrial/ clinical applications. In our study we have used ABAQUS FEA software to generate poroelastic displacements and strains under boundary conditions imitating the actual experiments in ultrasound elastography [46]. ABAQUS adopts effective stress principle to model the porous medium [47]. For complete details on the poroelastic simulation in ABAQUS, please refer [10]. We have used two samples from FEM simulation, Sample A and Sample B. In our FEM simulation, background mimics the normal tissue and the inclusion mimics a tumor. The simulated inclusion has a height of 40mm and radius of 20mm. The mechanical properties of the ABAQUS FEA simulated sample mimics the mechanical characteristics of the cancerous and healthy tissues [48] [49]. $1kPa$ stress was used to replicate the creep experiment. The simulated samples are squeezed from the top with constant stress while maintaining the bottom stable to create creep compression. Because of the noise model's importance in the estimation process, FEM samples were simulated for different input SNR values. Sample A has an inclusion of $0.75cm$ and Sample B has an inclusion of 1.02 cm. We have used initial values of $\eta = 0.02$ and $\tau = 10s$. The window of observation is $> 0.5\tau max$.

### 6.3 Performance Evaluation

For a given set of n trial estimates $\tau_i$, $1 \leq i \leq n$ done on a set of noisy samples from a time constant curve of known $\tau_i$, the bias is quantified as the difference between the mean of the measurements and the reference value in terms of percentage as shown in the equation [9].

$$Bias\% = \frac{|mean\,(\tau_i^{\wedge}) - \tau|}{\tau}\, X100 \tag{6.1}$$

Accuracy is given by the equation.

$$Accuracy\ \% = 100 - Bias\ \% \tag{6.2}$$

Quantitative performance measures such as Peak Signal-to-Noise Ratio (PSNR) has been used to estimate the performance of the discussed algorithm. PSNR is commonly used to measure the quality of reconstruction from noisy data [41]. The PSNR is defined as a ratio between the maximum possible power of a signal and the power of corrupting noise that affects the fidelity of its representation [41]. PSNR is usually expressed in terms of the logarithmic decibel scale. Mathematical equation for PSNR is given by,

$$PSNR_i = 10\log_{10}(\ \frac{Peakval_i^2}{MSE}) \tag{6.3}$$

where peakval is either specified by the user or taken from the input range. MSE is the mean square error

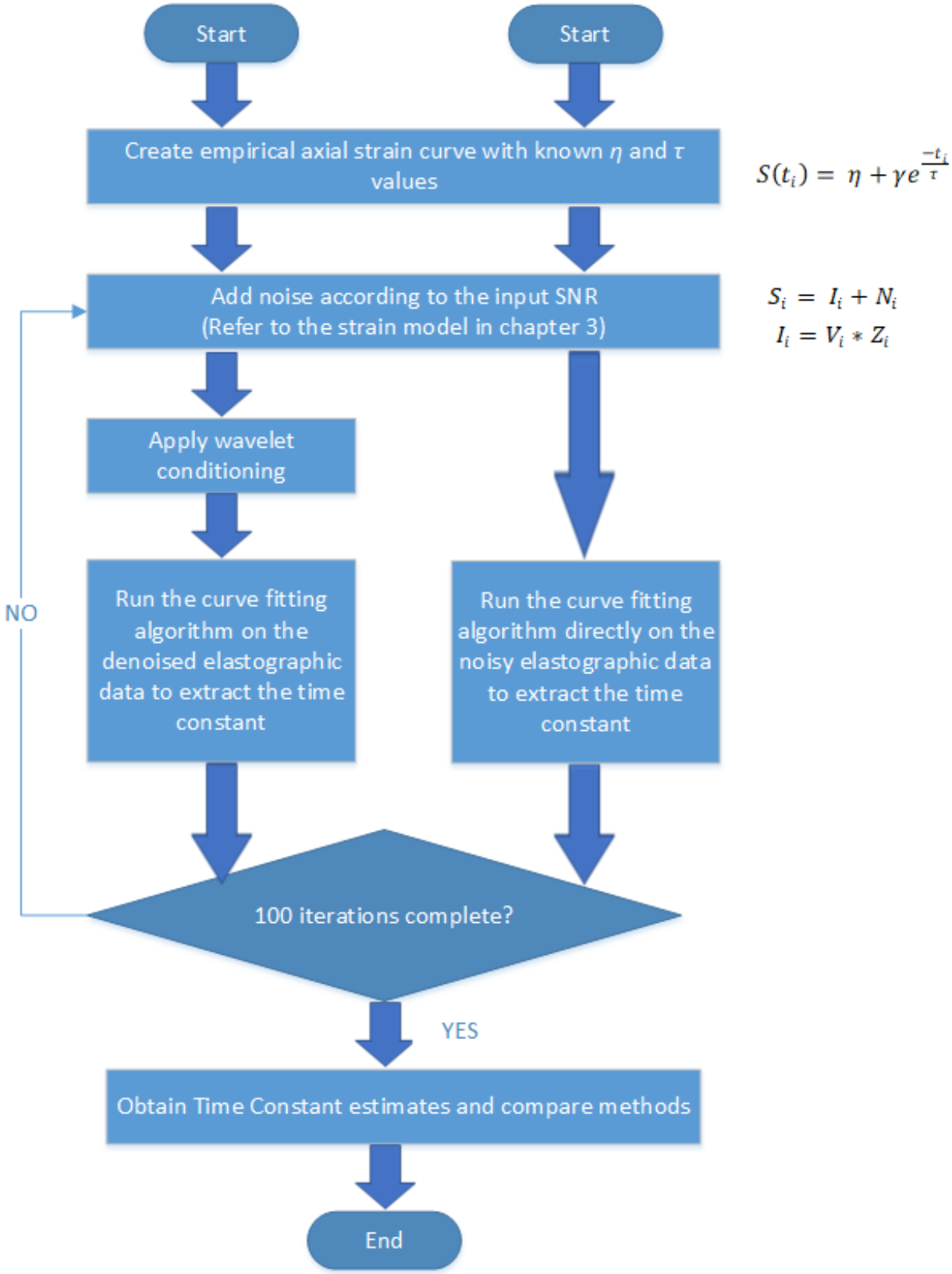


Figure 6.1: MATLAB Simulation Flow

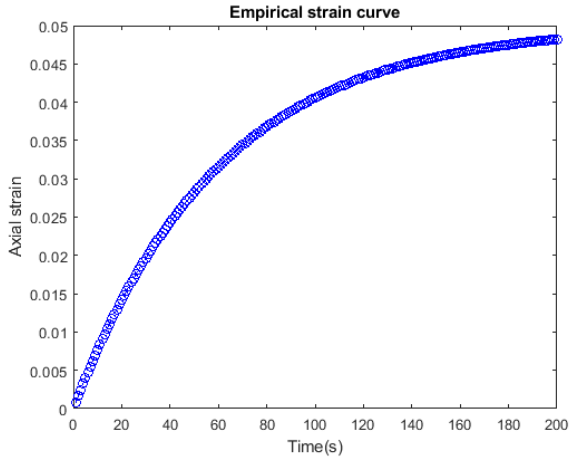


(a) Empirical strain curve

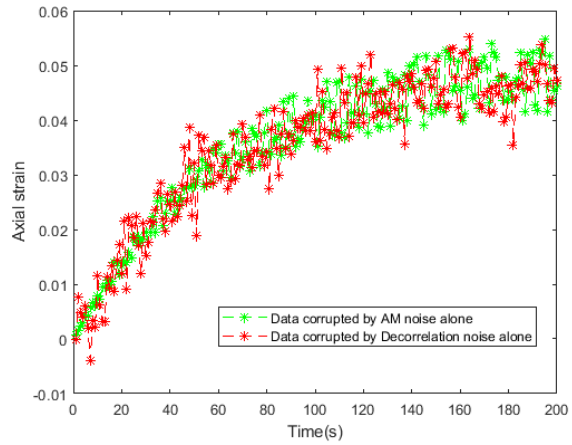


(b) Noisy curve obtained from a) after adding 1.AM noise, 2.Decorrelation noise

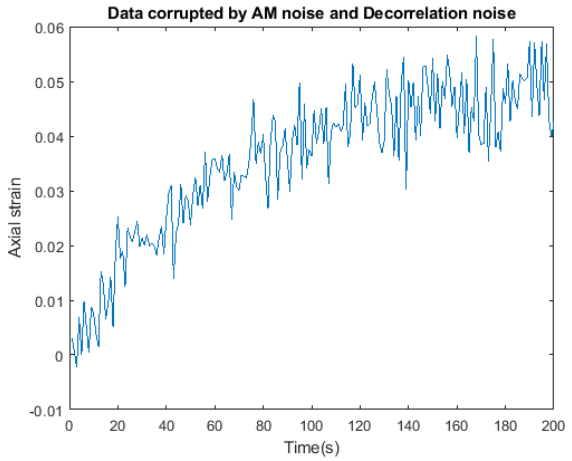


(c) Noisy curve obtained from a) after adding both the noise

Figure 6.2: Temporal strain curve

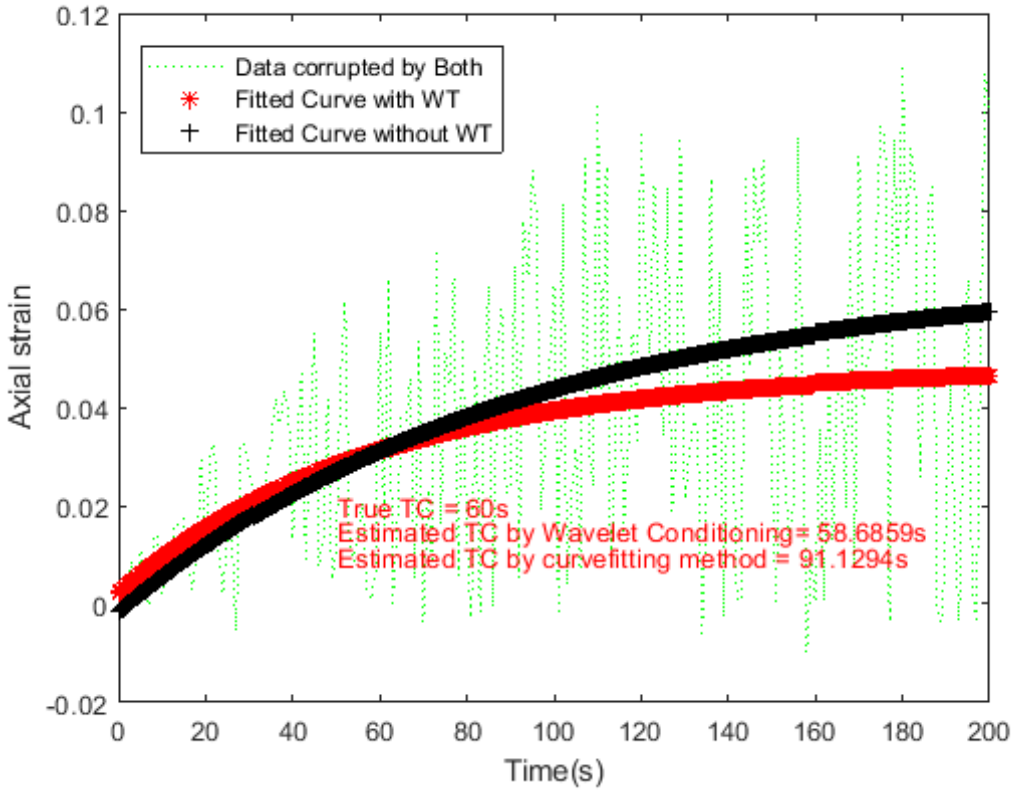


Figure 6.3: Example of a simulation run for comparison of curve fitting stand-alone method with the proposed method

# 7. SIMULATION RESULTS

## 7.1 MATLAB Simulation Results

### 7.1.1 ASTC Estimation With And Without Wavelet Denoising

*Curve fitting, Stand-Alone ASTC Estimator*

Figure 7.1 shows Curve fitting technique with LM optimization for ASTC constant estimation when elastographic data is corrupted only by decorrelation noise. For statistical analysis the simulation is repeated for different input SNR values of 10 20 30 40db. In the Figure 7.1 blue curve represents the theoretical curve for axial strain. The axial strain curve was created with $\eta = 0.25$ and 60s TC. The blue scattered points represent the elastographic data corrupted only by decorrelation noise. The red curve represents the fitted curve by LSE curve fitting technique along with LM optimization. As the signal improves and noise becomes less dominant the fitted curve becomes identical to theoretical curve in the absence of AM noise.

In absence of AM noise the curve fitting technique (discussed in chapter 04) works extremely well as an ASTC estimator with less than 1% error as seen in the Figure 7.1. For statistical analysis, 100 trials were run to estimate the true TC in presence of AM noise and in absence of AM noise by curve fitting method. For simulation, only additive Gaussian noise was added ensuring input SNR 10dB, 20dB, 30dB, 40db and 60db.

#### *7.1.1.1 Strain Data Corrupted By Decorrelation Noise Alone*

Single realization of CF with WC is compared with CF as a stand alone estimator in the Figure 7.2. As the signal improves and noise becomes less dominant the fitted curve becomes identical to theoretical curve in the absence of AM noise. The theoretical axial strain curve was created with $\eta = 0.05$ and TC = 60s.The red curve represents the fitted curve after wavelet conditioning while the black curve represents the fitted curve by CF stand alone method. The dotted green plot represents the noisy strain data. For statistical analysis, 100 trials were run and the bias% for both the methods and percentage error are recorded with respect to the true TC value in the Table

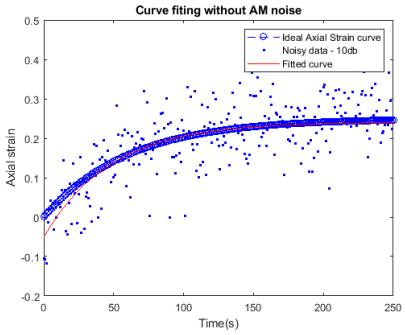


(a) Curve fitting with LM optimization for input SNR 10dB

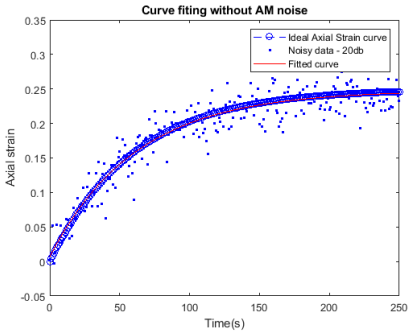


(b) Curve fitting with LM optimization for input SNR 20dB

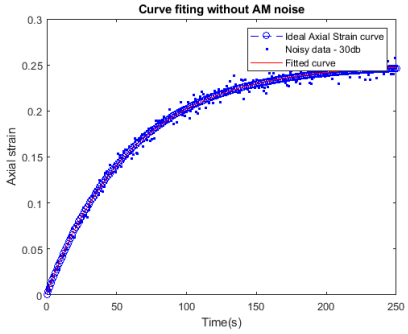


(c) Curve fitting with LM optimization for input SNR 30dB

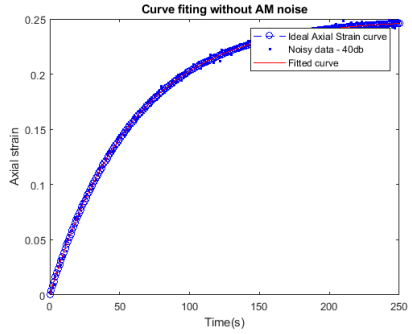


(d) Curve fitting with LM optimization for input SNR 40dB

Figure 7.1: LSE CF with LM Optimization applied over elastographic data corrupted by decorrelation noise for different input SNR

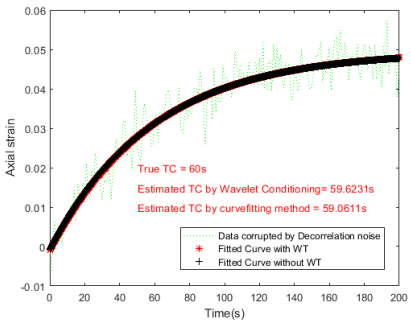


(a) Input SNR 20dB

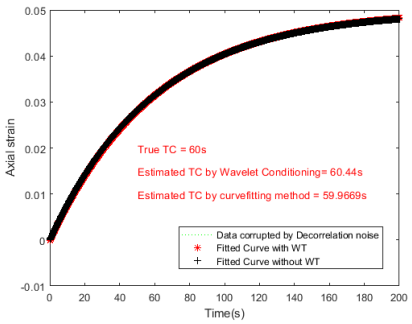


(b) Input SNR 60dB

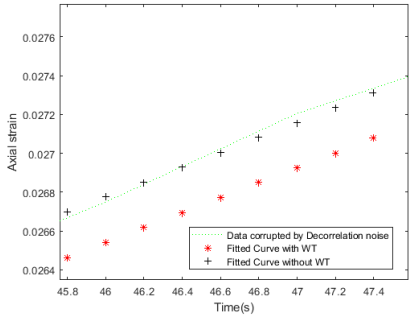


(c) b)Zoomed

Figure 7.2: Strain data corrupted by Decorrelation Noise alone

7.1. Plot 7.3 shows the accuracy of both the methods in presence of decorrelation noise alone. The accuracy of the CF as a stand alone estimator is comparable to CF with wavelet conditioning method.

| Input SNR | CF with WC | Stand-alone CF |
|---|---|---|
| 20db | 0.4838 | 1.6439 |
| 30db | 0.6943 | 0.9811 |
| 40db | 0.0249 | 0.2371 |
| 60db | 0.0742 | 0.0546 |

Table 7.1: Bias% in presence of decorrelation noise

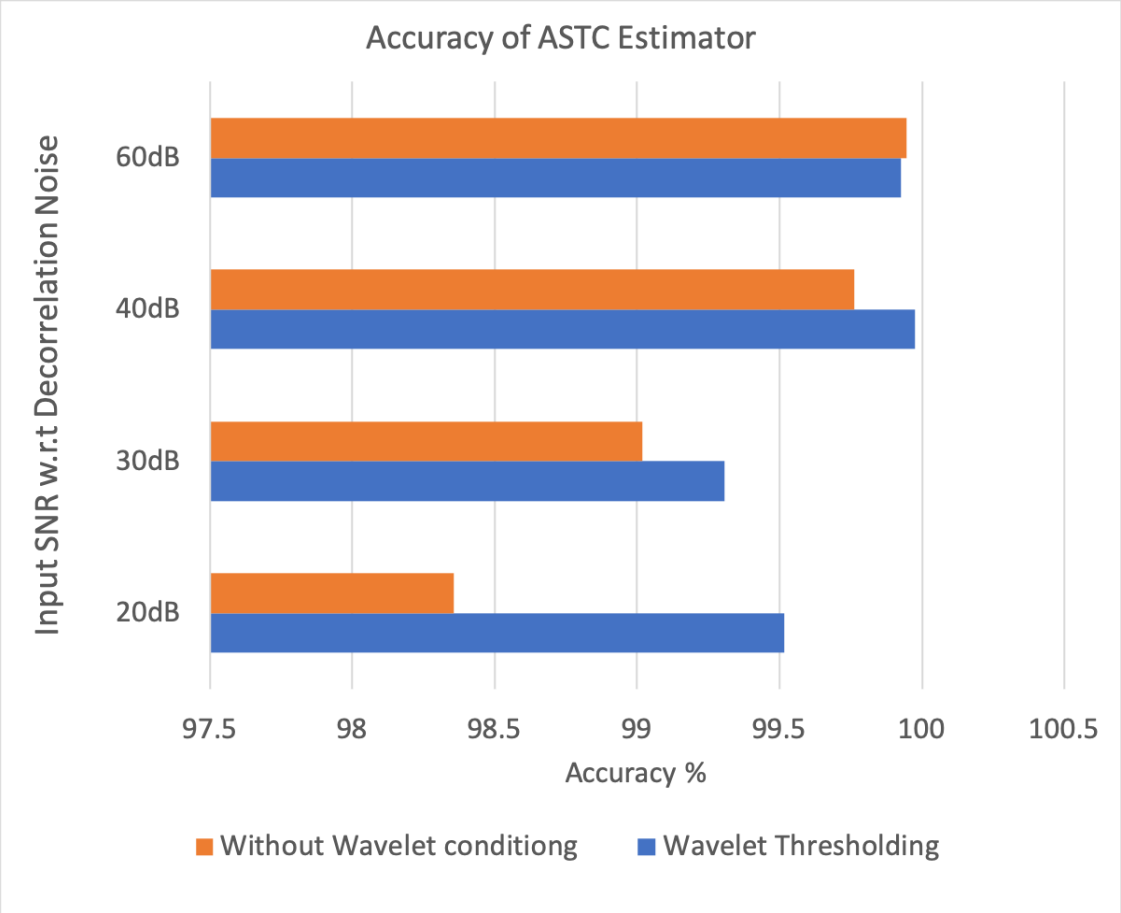


Figure 7.3: Accuracy% in presence of decorrelation noise

#### *7.1.1.2 Strain Data Corrupted By Multiplicative Noise Alone*

Single realization of CF with WC is compared with CF as a stand alone estimator in the Figure 7.4. As the signal improves and noise becomes less dominant, the fitted curve becomes closer to the theoretical curve. The theoretical axial strain curve was created with $\eta = 0.05$ and TC = 60s. The red curve represents the fitted curve after wavelet conditioning while the black curve represents the fitted curve by CF stand alone method. The dotted green plot represents the noisy strain data. For statistical analysis, 100 trials were run and the bias% for both the methods and percentage error are recorded with respect to the true TC value in the Table 7.2. Plot 7.5 shows the accuracy of both the methods in presence of AM noise alone. The accuracy of the Curve fitting with WC is 5 times better than stand alone CF method in estimating ASTC close to true value.

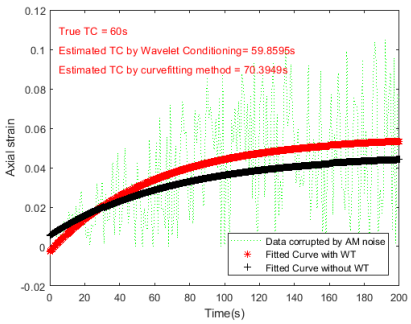


(a) Input SNR 20dB

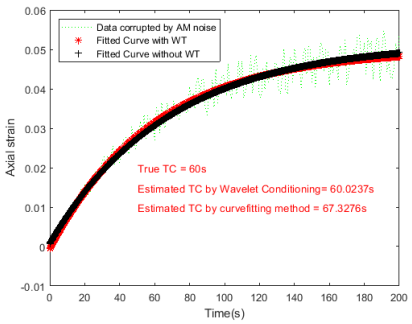


(b) Input SNR 60dB

Figure 7.4: Strain data corrupted by AM Noise alone

| Input SNR | CF with WC | Stand-alone CF |
|---|---|---|
| 20db | 1.9455 | 13.5 |
| 30db | 1.8 | 8.3 |
| 40db | 1.2 | 5.34 |
| 60db | 0.045 | 2.34 |

Table 7.2: Bias% in presence of AM noise

#### *7.1.1.3 Strain Data Corrupted By Additive And Multiplicative Noise*

Single realization of CF with WC is compared with CF as a stand alone estimator for different input SNR values in the Figure 7.6. Figure 7.6 a) - d) gives a comparison between curve fitting method without wavelet conditioning and curve fitting method with wavelet conditioning. The theoretical axial strain curve was created with $\eta = 0.05$ and TC = 60s. The red curve represents the fitted curve after wavelet conditioning while the black curve represents the fitted curve by CF stand alone method. The dotted green plot represents the noisy strain data. In the stand alone method we perform curve fitting directly on the noisy elastographic data. As the signal improves and noise becomes less dominant the fitted curve by CF technique without WC is still far from the theoretical curve, while the fitted curve from WC becomes almost identical to the theoretical strain curve. For statistical analysis, 100 trials were run and the bias% for both the methods and percentage error are recorded with respect to the true TC value in the Table 7.3. When curve fitting

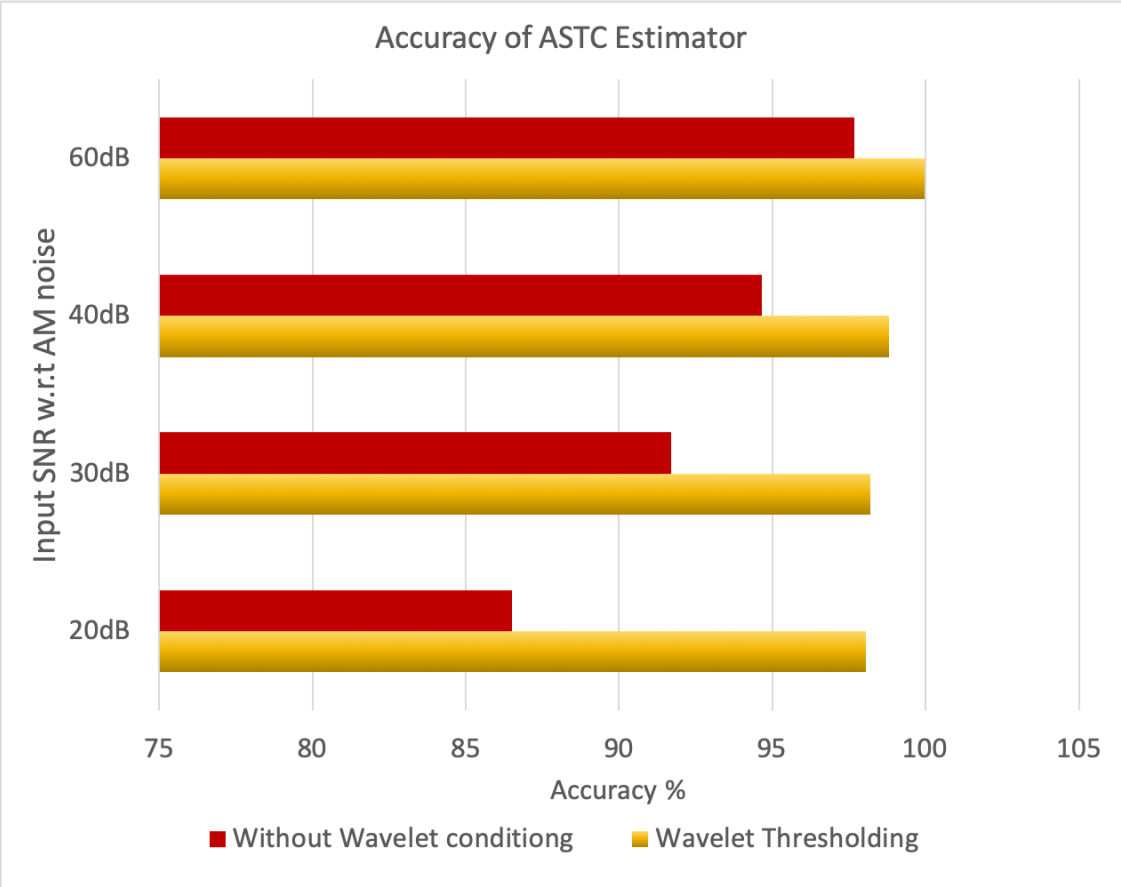


Figure 7.5: Accuracy% in presence of AM noise

is applied over denoised elastographic data instead of noisy elastographic data, it is possible to estimate ASTC values closer to true ASTC value. Plot 7.7 shows the accuracy of both the methods in presence of AM noise alone.

In the absence of AM noise the curve fitting technique (discussed in chapter 04) works extremely well as an ASTC estimator with less than 1% error. However, true axial strain ultrasound data is corrupted by other types of noise apart from decorrelation noise, for instance - AM noise. AM noise shifts the strain estimation from the center of the observation window, resulting in incorrect estimates. Unfortunately, the curve fitting technique lacks the ability to estimate ASTC with less than 1% error in the presence of AM noise when directly applied over noisy elastographic data which is evident from the Table 7.3. The error rate of curve fitting technique as a

stand-alone ASTC estimator is 10 times higher on an average compared to the error rate of curve fitting technique along with wavelet conditioning. Known issue with curve-fitting techniques when experimental data is extremely noisy, is that it creates extremely large local minima leading to significantly larger computations to find the global minimum and sometimes ends up finding only the local minimum, which is not necessarily the global minimum. By employing wavelet conditioning discussed in chapter 05, it is possible to avoid this scenario. Wavelet condition helps to smoothen the axial strain curve by filtering out most of the noisy components corrupting the elastographic data while trying to match the empirical strain curve.

| Input SNR | CF with WC | Stand-alone CF |
|---|---|---|
| 20db | 2.4455 | 39.1959 |
| 30db | 1.093 | 14.5268 |
| 40db | 0.2555 | 7.571 |
| 60db | 0.1296 | 3.3538 |

Table 7.3: Bias% in presence of AM noise

## 7.2 FEM Results

We have used FEM simulated sample A and sample B to validate our hypothesis. The simulated data presented in this study has a total of 200 frames of RF data for both the samples. Figure 7.8 shows the simulated axial strain data for frame 10, for Sample A and Sample B. The box on the Figure 7.8 shows the area inside the inclusion considered for analysis for all the 200 frames of RF data for the respective samples.

Table 7.4 shows the error rate associated with ASTC estimation with respect to the true TC value. The letter F in the table represents error rate greater than 30% in TC estimation. From Table 01 we can see that the Bias% error metric is relatively low for LM optimization when used with wavelet conditioning. From 7.4 and 7.5 for both sample A and Sample B we can say that the two step approach of wavelet conditioning along with curve fitting outperforms the stand - alone LM

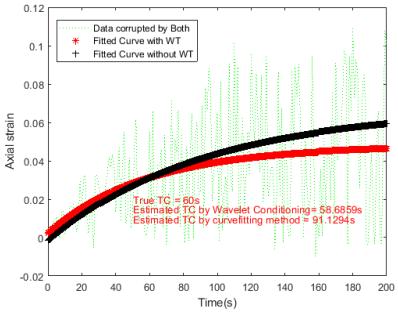


/

(a) Input SNR 20dB

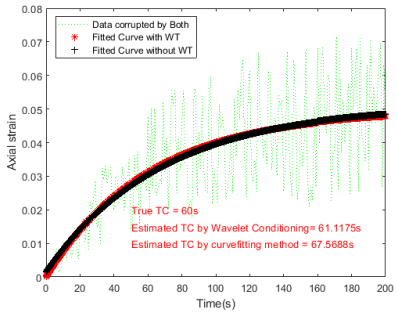


(b) Input SNR 30dB

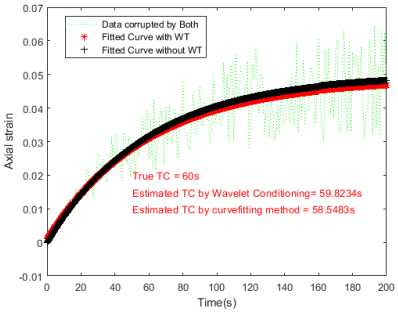


(c) Input SNR 40dB

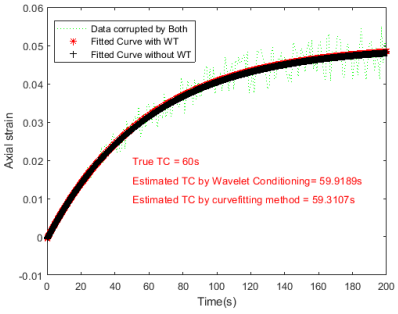


(d) Input SNR 60dB

Figure 7.6: Strain data corrupted by AM+Decorrelation Noise

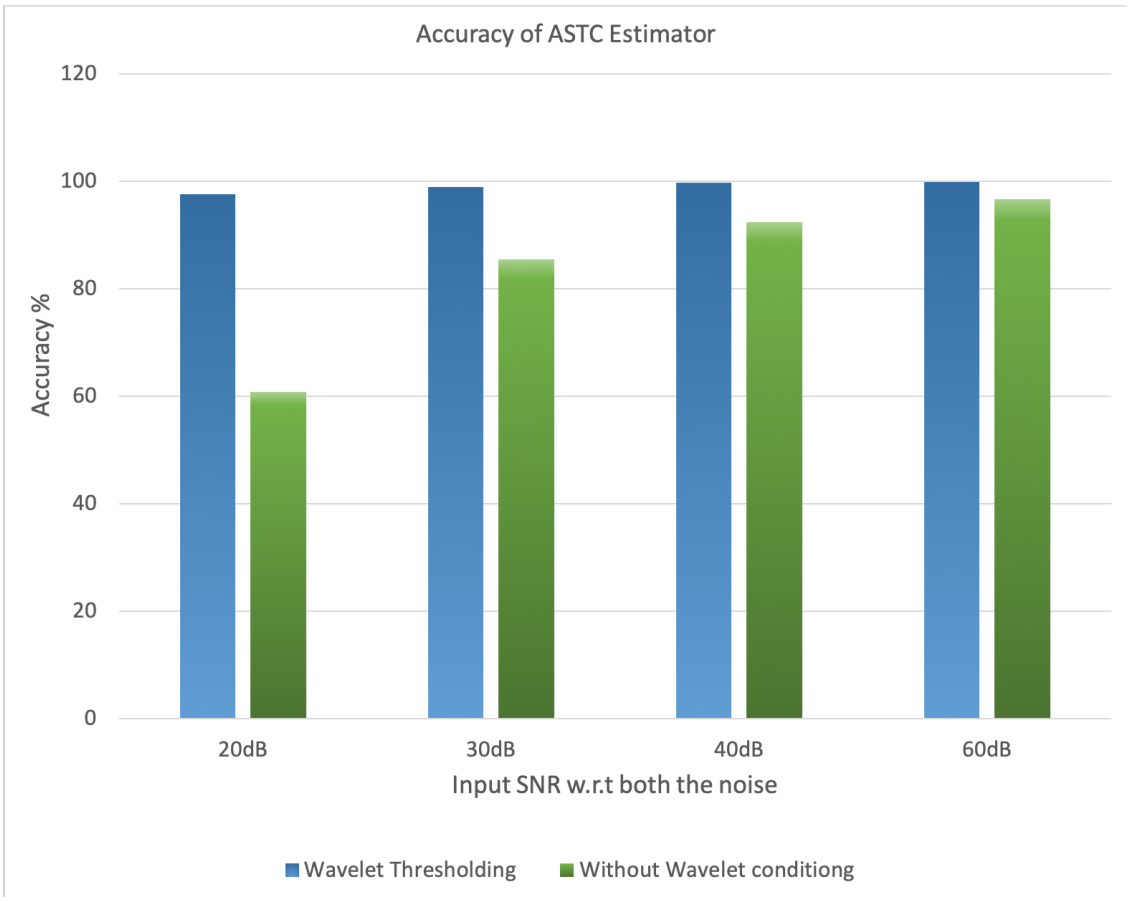


Figure 7.7: Accuracy% in presence of AM noise

curve fitting techniques. The wavelet conditioning along with LM curve fitting yields smaller error metric in ASTC estimation hence the better accuracy.From 7.4 and 7.5. It is evident that LSE+LM curve fitting is not robust in estimating ASTC.

| Input SNR | Wavelet Conditioning + LM (Hard Thresholding) | LM Stand-alone |
|---|---|---|
| 20db | 3.7917 | F |
| 30db | 3.0898 | F |
| 40db | 3.0209 | F |
| 60db | 2.8823 | F |

Table 7.4: SAMPLE A: BIAS% associated with ASTC estimation with respect to the true TC value

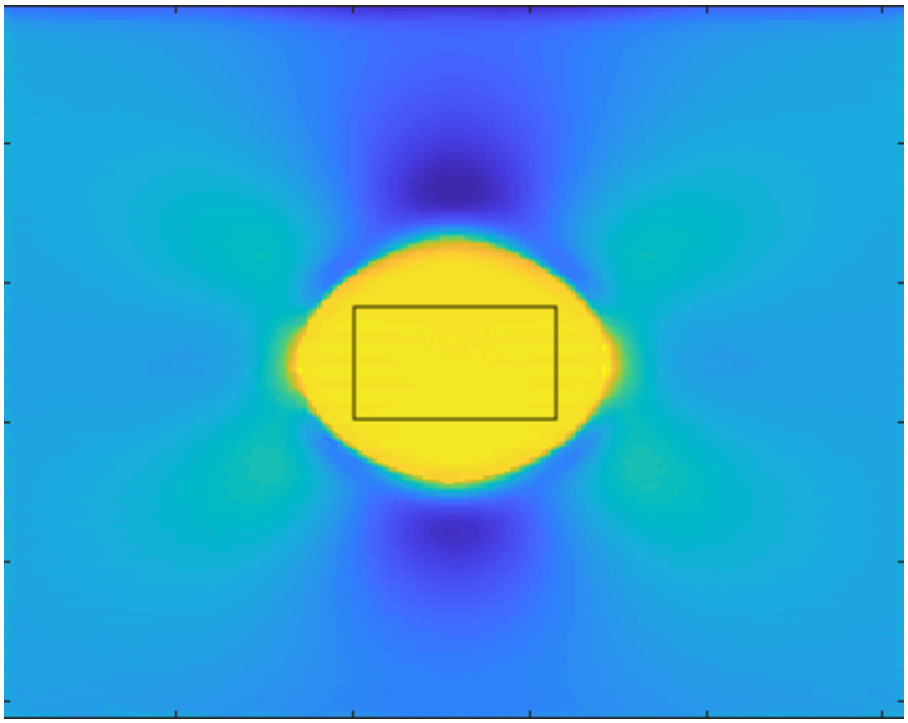

(a) Sample A

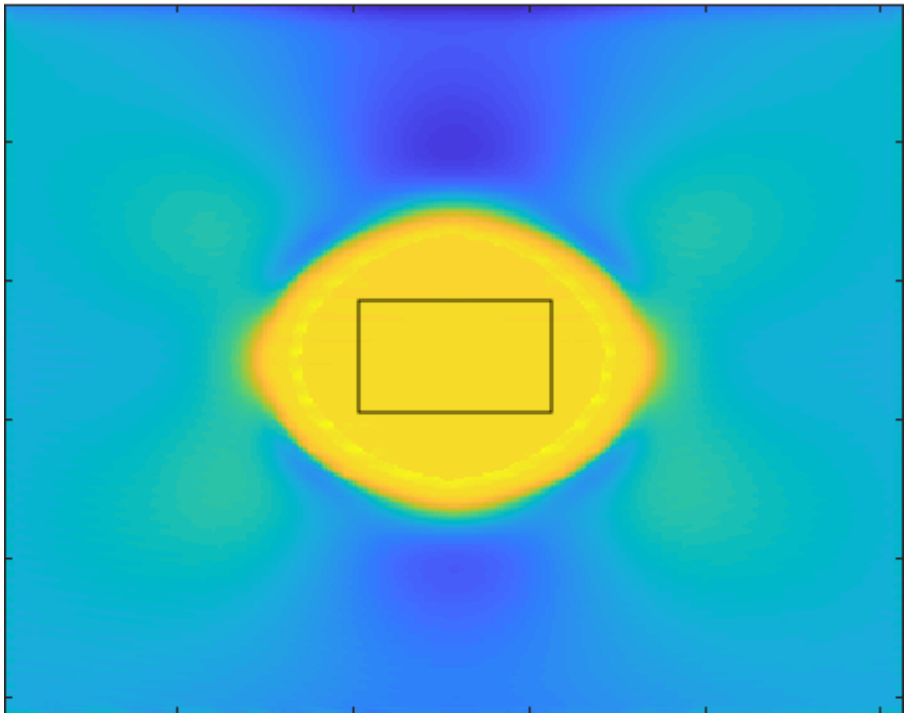

(b) Sample B

Figure 7.8: Simulated Strain data

| nput SNR | Wavelet Conditioning + LM (Hard Thresholding) | LM Stand-alone |
|---|---|---|
| 20db | 4.3301 | F |
| 30db | 4.0179 | 19.501 |
| 40db | 3.719 | 21.01 |
| 60db | 3.0396 | 20.95 |

Table 7.5: SAMPLE B: BIAS% associated with ASTC estimation with respect to the true TC value

Table 7.6 shows the error rate associated with ASTC estimation with respect to the true TC value using different wavelet kernel. Wavelet Kernel is used for estimating and designing wavelet filter coefficients for strain data analysis and synthesis. All the Wavelet families for different order was tested but only error for coif5, sym8, db1 or Haar, bior3.7 ( best in each family ) is shown in the Table 7.6. Table 7.7 shows the error rate associated with ASTC estimation with respect to the wavelet conditioning using different number of detail coefficients for computing inverse wavelet transform. Table 7.8 shows the error rate associated with ASTC estimation with respect to the wavelet conditioning using different number of wavelet decomposition before performing wavelet thresholding.

Table 7.9 gives a comparison between different filtering methods used to remove small noise remnants from the approximation wavelet coefficients and capture the signal components around the DC. Approximation coefficients contain significant signal components. Therefore, filter selection in wavelet domain becomes crucial to achieve high accuracy of ASTC estimator. Please note that these filters are also tested as stand-alone denoising method and all of them failed to converge expect low pass filter when used in Wavelet domain for any given input SNR value refer 7.9 7.10. The simulation was run on both the samples, A and B for different input SNR values.

Hard thresholding yields ASTC better estimates than soft thresholding for denoising the elastographic data when noise is very high, as the SNR improves they become almost identical to each other. Performance evaluation for WT is shown in Figure 7.9.

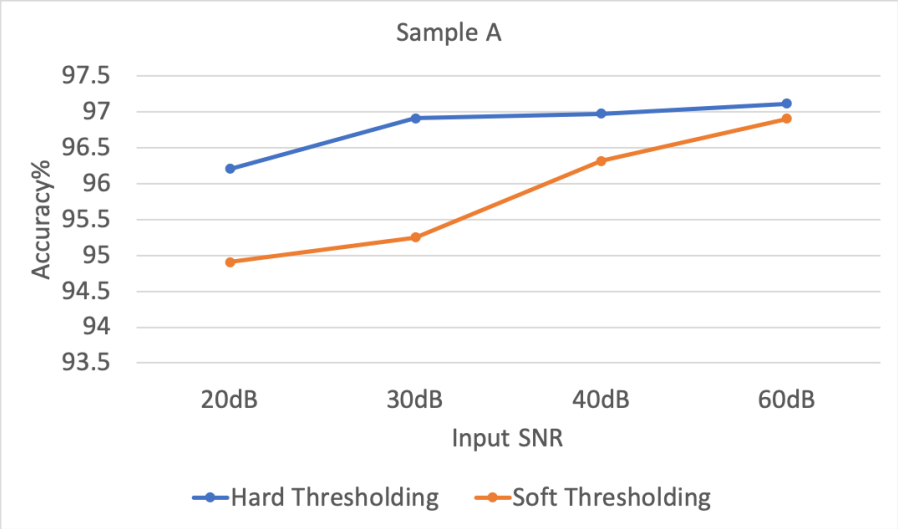


(a) Sample A

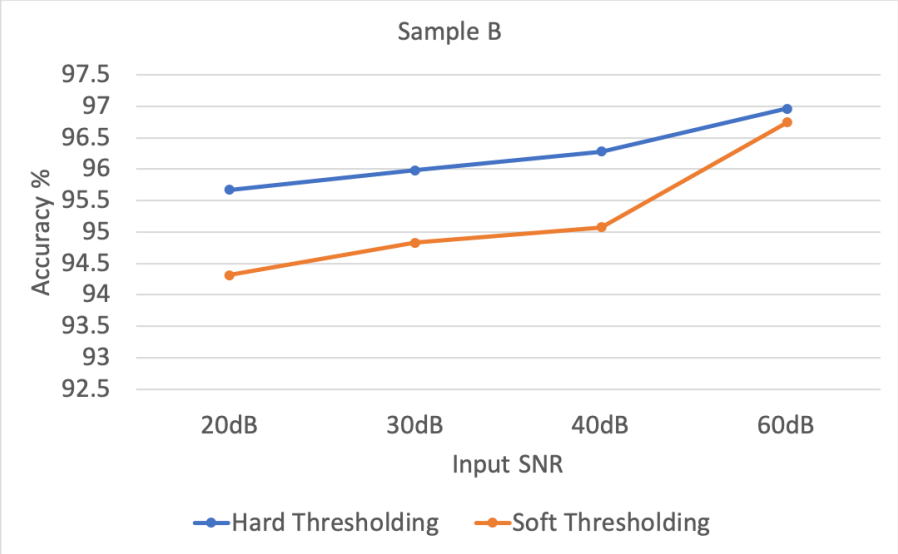


(b) Sample B

Figure 7.9: Accuracy with respect to wavelet thresholding

| Input SNR | Coiflets | Symlets | Daubechies | Biorthogonal |
|---|---|---|---|---|
| Sample A | | | | |
| 20dB | 12.8812 | 10.72 | 6.8576 | 3.7917 |
| 30dB | 11.4104 | 8.6287 | 6.8519 | 3.0898 |
| 40dB | 11.2507 | 8.6928 | 6.8542 | 3.0209 |
| 60dB | 10.8537 | 8.8796 | 6.8532 | 2.8823 |
| Sample B | | | | |
| 20dB | 11.8908 | 14.1756 | 6.8549 | 4.3301 |
| 30dB | 11.2197 | 14.6637 | 6.8519 | 4.0179 |
| 40dB | 11.0985 | 14.7635 | 6.6541 | 3.719 |
| 60dB | 10.7493 | 14.9903 | 6.8537 | 3.0396 |

Table 7.6: Wavelet Kernel comparison

| Input SNR | Only Last Level | 50% | 100% |
|---|---|---|---|
| Sample A | | | |
| 20dB | 3.7917 | 21.4936 | 22.1913 |
| 30dB | 3.0898 | 21.8639 | 21.7649 |
| 40dB | 3.0209 | 21.9017 | 21.909 |
| 60dB | 2.8823 | 22.0676 | 22.089 |
| Sample B | | | |
| 20dB | 4.3301 | 22.4564 | 24.424 |
| 30dB | 4.0179 | 22.3992 | 23.6478 |
| 40dB | 3.719 | 22.3979 | 23.6933 |
| 60dB | 3.0396 | 22.4564 | 23.7609 |

Table 7.7: Inverse Wavelet Transform with few detail coefficients

Quantitative performance measure such as PSNR has been used to estimate the performance of the denoising algorithm. PSNR is commonly used to measure the quality of reconstruction data from noisy data from wavelet transform. In our study, we use the reconstructed data to estimate the TC using curve fitting method. Table 7.11 shows the PSNR of the reconstructed data for different input SNR values. The denoising algorithm is pretty consistent irrespective of different input SNR values .

| Decomposition Level | Bias% |
|---|---|
| Sample A | |
| 1 | F |
| 2 | F |
| 4 | F |
| log2 N | 2.883 |
| Sample B | |
| 1 | F |
| 2 | F |
| 4 | 19.501 |
| log2 N | 3.0396 |

Table 7.8: Wavelet Decomposition Level Selection for Input SNR 60dB

| SNR | Median Filter | Low pass Filter | Gaussian Filter | Linear filter | Guided Filter |
|---|---|---|---|---|---|
| Sample A | | | | | |
| 20db | F | 3.7917 | F | F | F |
| 30db | F | 3.0898 | F | F | F |
| 40db | F | 3.0209 | F | F | F |
| 60db | F | 2.8823 | F | F | F |
| Sample B | | | | | |
| 20db | F | 4.3301 | F | F | F |
| 30db | F | 4.0179 | F | F | F |
| 40db | F | 3.719 | F | F | F |
| 60db | F | 3.0396 | F | F | F |

Table 7.9: Bias% : Wavelet Conditioning (Hard thresholding) + LM

Estimated ASTC elastograms for an heterogeneous poroelastic sample A, Figure 7.10 and sample B, Figure 7.11 for different input SNR from FE simulation is shown in the figure. From the Figure 7.10, we see that the ASTC elastogram computed by the proposed technique is closer to the ground truth, refer Table 7.4 and 7.5, relative to the ASTC images computed by stand-alone Curve fitting method. Wavelet conditioning improves the robustness of curve fitting technique.

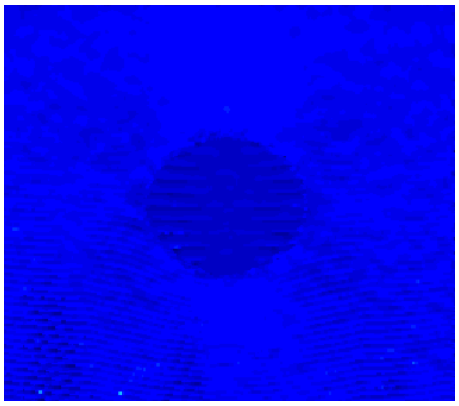

(a) ASTC Elastogram : Curve fitting, Stand Alone - 20db Input SNR

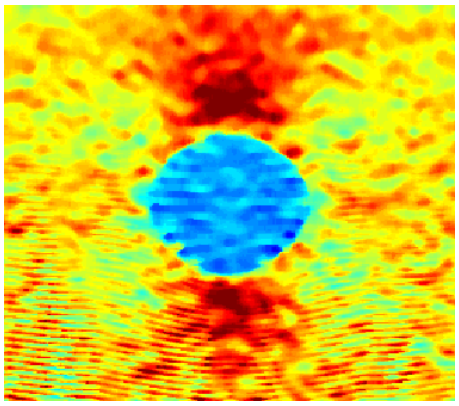

(b) ASTC Elastogram : Curve fitting with Wavelet Conditioning - 20db Input SNR

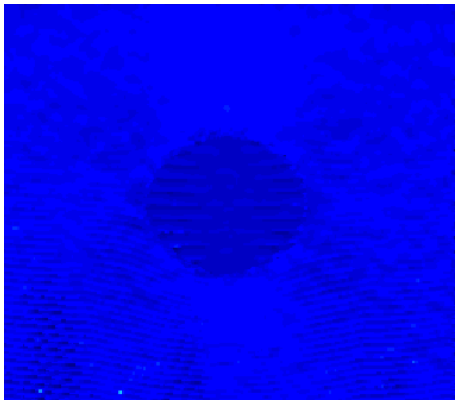

(c) ASTC Elastogram : Curve fitting, Stand Alone - 60db Input SNR

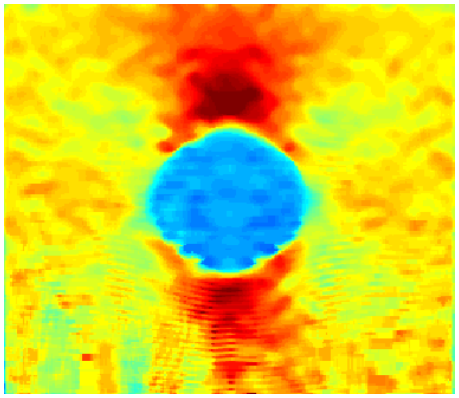

(d) ASTC Elastogram : Curve fitting with Wavelet Conditioning - 60db Input SNR

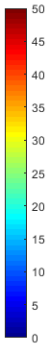


(e) Color scale

Figure 7.10: Sample A: ASTC Elastogram for Input SNR 20dB and 60dB

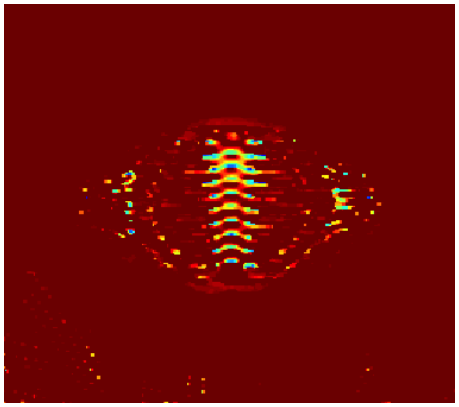

(a) ASTC Elastogram : Curve fitting, Stand Alone - 20db Input SNR

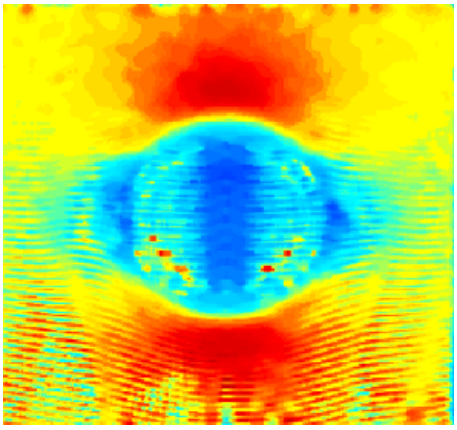

(b) ASTC Elastogram : Curve fitting with Wavelet Conditioning - 20db Input SNR

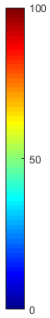


Figure 7.11: Sample B: ASTC Elastogram for Input SNR 20dB and 60dB

| SNR | Median Filter | Low pass Filter | Gaussian Filter | Linear filter | Guided Filter |
|---|---|---|---|---|---|
| Sample A | | | | | |
| 20db | F | 5.0944 | F | F | F |
| 30db | F | 4.747 | F | F | F |
| 40db | F | 3.6846 | F | F | F |
| 60db | F | 3.0936 | F | F | F |
| Sample B | | | | | |
| 20db | F | 5.6858 | F | F | F |
| 30db | F | 5.1678 | F | F | F |
| 40db | F | 4.9256 | F | F | F |
| 60db | F | 3.2538 | F | F | F |

Table 7.10: Bias% : Wavelet Conditioning (Soft thresholding) + LM

| SNR Input | PSNR |
|---|---|
| Sample A | |
| 20 dB | 88.7489 |
| 30 dB | 89.9207 |
| 40 dB | 90.1406 |
| 60 dB | 90.1902 |
| Sample B | |
| 20 dB | 87.7256 |
| 30 dB | 89.8993 |
| 40 dB | 90.1347 |
| 60 dB | 91.1808 |

Table 7.11: PSNR of denoised data after Wavelet Conditioning (Hard Thresholding)

# 8. EXPERIMENT AND RESULTS

## 8.1 In vivo Experimental Method

Data from an animal subject with triple negative breast cancer [50] are used for our study. We have used, mouse as our animal subject to acquire experimental data. With a variety of clinical models available, breast cancer development can be researched in mouse. Many clinical models may be helpful in investigating certain elements of the advancement of cancer but unfortunately, they do not epitomize the whole cancer cycle. The best way to mimic human cancerous disease in mice is by injecting the cancerous cells beneath the mouse's mammary fat pad [50]. The in vivo data acquisition protocol was approved by the Houston Methodist Research Institute, Institutional Animal Care and Use Committee.

The elastography experiments were conducted using Sonix RP, an ultrasound diagnostic system with Windows XP Operating System. It is a product by Ultrasonix, Canada. The transducer used for these experiments was a 38 mm real-time linear array with 128 elements, a bandwidth between 5-14 MHz, a center frequency of 6.6 MHz, 50% fractional bandwidth (at -6 dB), a sampling frequency of 40 MHz, and a 1 mm beam width at the focus point. To compensate for the surface geometry as well as improve the focus inside the fairly superficial tumor in the mouse, an aqueous ultrasound gel pad (Aquaflex, Parker Laboratories, NJ, USA) was placed between the compressor plate and the animal. Creep experiments were performed manually on the anesthetized animal. A constant force, replicating the effects of a creep test, was applied to the anesthetized animal through the weight of the transducer, compressor plate, and a weight band. As described in Chapter 03, the axial strain $S_i$ is computed in a cumulative manner using consecutive frames to maintain an acceptable correlation level [9]. Temporal changes in the axial strain distribution can be estimated pixel by pixel. From the temporal curves of the axial strain, the axial strain time constant for each pixel in the elastograms can be computed. A TC elastogram, or a map of the local time constants, can be created for the entire image. Ultrasound RF data were acquired for up to 1 min. Multiple

data acquisitions were performed at different locations around the tumor. Data could not be collected consecutively at the highest frame rate of the ultrasonic system because the system has a buffer that limits the total number of frames that can be acquired during a single collection. TC elastograms were computed for the in vivo data using all 485 frames available.

## 8.2 In vivo Experimental Result

The ASTC elastogram computed from invivo experiment using curve fitting along with wavelet conditioning is shown in the Figure 8.2. These findings demonstrate the technical feasibility of using the wavelet conditioning prior to LM algorithm to produce ASTC on actual experimental invivo axial strain data. The estimated ASTC for invivo experiments was 10-30s within the inclusion and 20-70s outside the inclusion (refer Figure 8.1)[46].

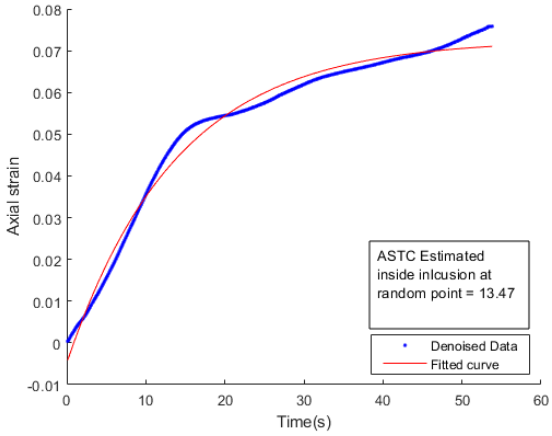


(a) Inside Inclusion

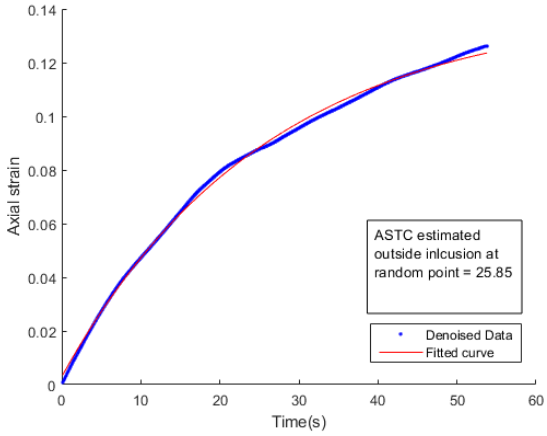


(b) Outside Inclusion

Figure 8.1: Strain curve inside and outside inclusion

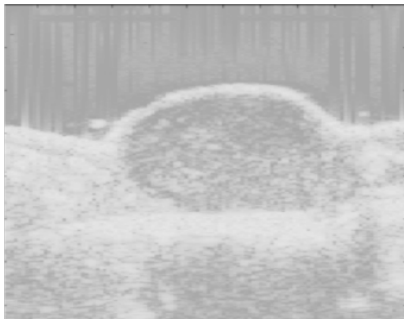

(a) B-MODE Image

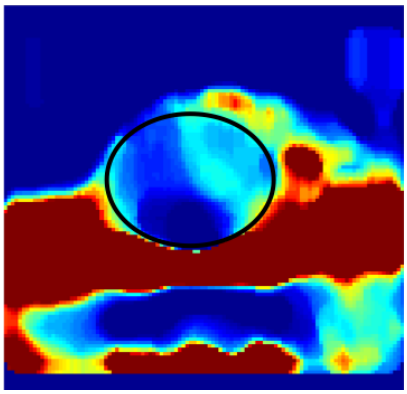

(b) Invivo ASTC Elastogram


(c) Scale

Figure 8.2: Invivo B-mode image and Axial Strain Time Constant Elastogram

# 9. CONCLUSION

In this study, we have proposed a 2-step approach for estimating the ASTC from the elastographic strain data of the poroelastic soft tissue. In this study we show how denoising elastographic strain data prior to curve fitting will increase the robustness of curve fitting technique and also increase the accuracy of the estimated ASTC. We have tested wavelet thresholding as a stand-alone algorithm to remove AM noise and have used PSNR metric to evaluate the performance of the algorithm. We have compared the performance of wavelet thresholding + curve fitting method in estimating the ASTC elastogram with the stand-alone curve fitting estimation method for a wide range of input SNRs, for all cases the proposed (wavelet thresholding + curve fitting) ASTC estimator produced accurate and reliable results. We observed that our proposed technique can estimate the ASTC with greater accuracy in most cases relative to the stand-alone curve fitting method which failed to converge for the simulated axial strain elastographic data. In this study, experimental data were used as a proof of concept to validate the observations of the simulation. As ASTC can be linked directly to human soft tissue's mechanical attributes, the 2-step approach of estimating the ASTC by curve fitting technique along with wavelet thresholding may be useful in diagnosis of malignancy, clinical guidance about the state or presence of the disease, severity of the disease and status of the tissue under treatment. This study mainly focused on ASTC estimation, the proposed 2-step approach can be extended to estimate equilibrium strain as well as EPR TC from the noisy elastographic data. The denoising algorithm used in this study is generic and can be extended to any elastographic parameter estimator currently available in the field.

REFERENCES


[1] J.-L. Gennisson, T. Deffieux, M. Fink, and M. Tanter, "Ultrasound elastography: principles and techniques," *Diagnostic and interventional imaging*, vol. 94, no. 5, pp. 487–495, 2013.

[2] R. Righetti, M. Righetti, J. Ophir, and T. A. Krouskop, "The feasibility of estimating and imaging the mechanical behavior of poroelastic materials using axial strain elastography," *Physics in Medicine & Biology*, vol. 52, no. 11, p. 3241, 2007.

[3] R. M. Sigrist, J. Liau, A. El Kaffas, M. C. Chammas, and J. K. Willmann, "Ultrasound elastography: review of techniques and clinical applications," *Theranostics*, vol. 7, no. 5, p. 1303, 2017.

[4] S. Srinivasan, T. Krouskop, and J. Ophir, "Comparing elastographic strain images with modulus images obtained using nanoindentation: preliminary results using phantoms and tissue samples," *Ultrasound in medicine & biology*, vol. 30, no. 3, pp. 329–343, 2004.

[5] C. Armstrong, W. Lai, and V. Mow, "An analysis of the unconfined compression of articular cartilage," *Journal of biomechanical engineering*, vol. 106, no. 2, pp. 165–173, 1984.

[6] J. Gore, A. Anderson, M. Does, D. Gochberg, J. Joers, R. Kennan, E. Parsons, and M. Schachter, "The relationship of problems in biomedical mri to the study of porous media," *Magnetic resonance imaging*, vol. 19, no. 3-4, pp. 295–300, 2001.

[7] H. P. G. Darcy, *Les Fontaines publiques de la ville de Dijon. Exposition et application des principes à suivre et des formules à employer dans les questions de distribution d'eau, etc*. V. Dalamont, 1856.

[8] E. E. Konofagou, T. P. Harrigan, J. Ophir, and T. A. Krouskop, "Poroelastography: Imaging the poroelastic properties of tissues," *Ultrasound in medicine & biology*, vol. 27, no. 10, pp. 1387–1397, 2001.

[9] S. P. Nair, X. Yang, T. A. Krouskop, and R. Righetti, "Performance analysis of a new real-time elastographic time constant estimator," *IEEE transactions on medical imaging*, vol. 30, no. 2, pp. 497–511, 2011.

[10] M. T. Islam, A. Chaudhry, G. Unnikrishnan, J. Reddy, and R. Righetti, "An analytical poroelastic model for ultrasound elastography imaging of tumors," *Physics in Medicine & Biology*, vol. 63, no. 2, p. 025031, 2018.

[11] M. T. Islam and R. Righetti, "A novel filter for accurate estimation of fluid pressure and fluid velocity using poroelastography," *Computers in biology and medicine*, vol. 101, pp. 90–99, 2018.

[12] J. Ophir, I. Cespedes, H. Ponnekanti, Y. Yazdi, and X. Li, "Elastography: a quantitative method for imaging the elasticity of biological tissues," *Ultrasonic imaging*, vol. 13, no. 2, pp. 111–134, 1991.

[13] M. O'Donnell, A. R. Skovoroda, B. M. Shapo, and S. Y. Emelianov, "Internal displacement and strain imaging using ultrasonic speckle tracking," *IEEE transactions on ultrasonics, ferroelectrics, and frequency control*, vol. 41, no. 3, pp. 314–325, 1994.

[14] M. O'Donnell, A. Skovorada, and B. Shapo, "Measurement of arterial wall motion using fourier based speckle tracking algorithms," in *IEEE 1991 Ultrasonics Symposium,*, pp. 1101–1104, IEEE, 1991.

[15] T. Krouskop, D. Dougherty, F. Vinson, *et al.*, "A pulsed doppler ultrasonic system for making noninvasive measurements of the mechanical properties of soft tissue," *J Rehabil Res Dev*, vol. 24, no. 2, pp. 1–8, 1987.

[16] R. Lerner, "Sono-elasticity in ultrasonic tissue characterization and echographic imaging," in *Proc. 7th Eur. Comm. Workshop, Nijmegen, The Netherlands, 1987*, 1987.

[17] R. M. Lerner, S. Huang, and K. J. Parker, "âĂIJsonoelasticityâĂİ images derived from ultrasound signals in mechanically vibrated tissues," *Ultrasound in medicine & biology*, vol. 16, no. 3, pp. 231–239, 1990.

[18] Y. Yamakoshi, J. Sato, and T. Sato, "Ultrasonic imaging of internal vibration of soft tissue under forced vibration," *IEEE transactions on ultrasonics, ferroelectrics, and frequency control*, vol. 37, no. 2, pp. 45–53, 1990.

[19] S. K. Alam, D. W. Richards, and K. J. Parker, "Detection of intraocular pressure change in the eye using sonoelastic doppler ultrasound," *Ultrasound in medicine & biology*, vol. 20, no. 8, pp. 751–758, 1994.

[20] J. Ophir, S. K. Alam, B. Garra, F. Kallel, E. Konofagou, T. Krouskop, and T. Varghese, "Elastography: ultrasonic estimation and imaging of the elastic properties of tissues," *Proceedings of the Institution of Mechanical Engineers, Part H: Journal of Engineering in Medicine*, vol. 213, no. 3, pp. 203–233, 1999.

[21] J. Ophir, S. Srinivasan, R. Righetti, and A. Thittai, "Elastography: A decade of progress (2000-2010)," *Current Medical Imaging Reviews*, vol. 7, no. 4, pp. 292–312, 2011.

[22] M. T. Islam, A. Chaudhry, S. Tang, E. Tasciotti, and R. Righetti, "A new method for estimating the effective poissonâĂŹs ratio in ultrasound poroelastography," *IEEE transactions on medical imaging*, vol. 37, no. 5, pp. 1178–1191, 2018.

[23] G. P. Berry, J. C. Bamber, C. G. Armstrong, N. R. Miller, and P. E. Barbone, "Towards an acoustic model-based poroelastic imaging method: I. theoretical foundation," *Ultrasound in medicine & biology*, vol. 32, no. 4, pp. 547–567, 2006.

[24] R. Righetti, J. Ophir, S. Srinivasan, and T. A. Krouskop, "The feasibility of using elastography for imaging the poisson's ratio in porous media," *Ultrasound in medicine & biology*, vol. 30, no. 2, pp. 215–228, 2004.

[25] R. Righetti, S. Srinivasan, A. T. Kumar, J. Ophir, and T. A. Krouskop, "Assessing image quality in effective poisson's ratio elastography and poroelastography: I," *Physics in Medicine & Biology*, vol. 52, no. 5, p. 1303, 2007.

[26] Y. P. Samarin, "Derivation of exponential approximations for creep curves by the method of successive isolation of exponential terms," *Strength of Materials*, vol. 6, no. 9, pp. 1062–1066, 1974.

[27] Y.-C. Fung, "Bio-viscoelastic solids," in *Biomechanics*, pp. 196–260, Springer, 1981.

[28] J. Nilsson and S. Riedel, "Sinusoidal steady-state analysis," *Electric Circuits*, vol. 7, pp. 380–447, 2005.

[29] S. Cui and D. C. Liu, "Noise reduction for ultrasonic elastography using transmit-side frequency compounding: A preliminary study," *IEEE transactions on ultrasonics, ferroelectrics, and frequency control*, vol. 58, no. 3, pp. 509–516, 2011.

[30] J. E. Lindop, G. M. Treece, A. H. Gee, and R. W. Prager, "Estimation of displacement location for enhanced strain imaging," *IEEE Transactions on Ultrasonics, Ferroelectrics, and Frequency Control*, vol. 54, no. 9, pp. 1751–1771, 2007.

[31] H. Rivaz, E. M. Boctor, M. A. Choti, and G. D. Hager, "Real-time regularized ultrasound elastography," *IEEE transactions on medical imaging*, vol. 30, no. 4, pp. 928–945, 2011.

[32] A. Ranganathan, "The levenberg-marquardt algorithm," *Tutoral on LM algorithm*, vol. 11, no. 1, pp. 101–110, 2004.

[33] K. Levenberg, "A method for the solution of certain non-linear problems in least squares," *Quarterly of applied mathematics*, vol. 2, no. 2, pp. 164–168, 1944.

[34] D. W. Marquardt, "An algorithm for least-squares estimation of nonlinear parameters," *Journal of the society for Industrial and Applied Mathematics*, vol. 11, no. 2, pp. 431–441, 1963.

[35] M. N. Ali, "A wavelet-based method for mri liver image denoising," *Biomedical Engineering/Biomedizinische Technik*, 2019.

[36] S. Khan, A. Jain, and A. Khare, "Image denoising based on adaptive wavelet thresholding by using various shrinkage methods under different noise condition," *International Journal of Computer Applications*, vol. 59, no. 20, 2012.

[37] R. Sivakumar and D. Nedumaran, "Comparative study of speckle noise reduction of ultrasound b-scan images in matrix laboratory environment," *International Journal of Computer Applications*, vol. 10, no. 9, pp. 46–50, 2010.

[38] MATLAB, "Wavelet toolbox documentation," 2019.

[39] K. Z. Abd-Elmoniem, A.-B. Youssef, and Y. M. Kadah, "Real-time speckle reduction and coherence enhancement in ultrasound imaging via nonlinear anisotropic diffusion," *IEEE Transactions on Biomedical Engineering*, vol. 49, no. 9, pp. 997–1014, 2002.

[40] M. Mastriani, "New wavelet-based superresolution algorithm for speckle reduction," in *in SAR Images,âĂİ International Journal of Computer Science*, Citeseer, 2006.

[41] M. Mastriani, "Denoising and compression in wavelet domain via projection onto approximation coefficients," in *International Journal of Information and Communication Engineering*, Citeseer, 2009.

[42] N. Mustafa, S. A. Khan, J.-P. Li, M. Khalil, K. Kumar, and M. Giess, "Medical image denoising schemes using wavelet transform with fixed form thresholding," in *2014 11th International Computer Conference on Wavelet Actiev Media Technology and Information Processing (ICCWAMTIP)*, pp. 397–402, IEEE, 2014.

[43] D. L. Donoho, "De-noising by soft-thresholding," *IEEE transactions on information theory*, vol. 41, no. 3, pp. 613–627, 1995.

[44] Y. S. Kim and J. B. Ra, "Improvement of ultrasound image based on wavelet transform: speckle reduction and edge enhancement," in *Medical Imaging 2005: Image Processing*, vol. 5747, pp. 1085–1093, International Society for Optics and Photonics, 2005.

[45] D. Gnanadurai and V. Sadasivam, "An efficient adaptive thresholding technique for wavelet based image denoising," *International Journal of Signal Processing*, vol. 2, no. 2, pp. 114–119, 2006.

[46] M. T. Islam, A. Chaudhry, and R. Righetti, "A robust method to estimate the time constant of elastographic parameters," *IEEE transactions on medical imaging*, 2019.

[47] K. Hibbitt, "Sorensen, inc. abaqus/explicit user's manual, version 6.5. 1," 2005.

[48] M. Sridhar, J. Liu, and M. Insana, "Viscoelasticity imaging using ultrasound: parameters and error analysis," *Physics in Medicine & Biology*, vol. 52, no. 9, p. 2425, 2007.

[49] R. Leiderman, P. E. Barbone, A. A. Oberai, and J. C. Bamber, "Coupling between elastic strain and interstitial fluid flow: ramifications for poroelastic imaging," *Physics in Medicine & Biology*, vol. 51, no. 24, p. 6291, 2006.

[50] R. Palomba, A. Parodi, M. Evangelopoulos, S. Acciardo, C. Corbo, E. De Rosa, I. Yazdi, S. Scaria, R. Molinaro, N. T. Furman, *et al.*, "Biomimetic carriers mimicking leukocyte plasma membrane to increase tumor vasculature permeability," *Scientific reports*, vol. 6, p. 34422, 2016.